Journal of Materials Science & Technology 210 (2025) 188–194

Contents lists available at ScienceDirect

Journal of Materials Science & Technology

journal homepage: www.elsevier.com/locate/jmst

Letter

# Ultrafast pressure sintering of $B_4C$-based composites via direct Joule heating

## 1. Introduction

$B_4C$ ceramics have high potential for use in aerospace, military, nuclear energy, and other fields owing to their excellent properties such as low density, high melting point, high hardness, high chemical stability, excellent wear resistance, and good neutron absorption ability [1–3]. However, the fracture toughness (1.9 MPa·$m^{1/2}$) of $B_4C$ is poor [2]. Furthermore, the low diffusion coefficient associated with the strong covalent bond of $B_4C$ makes it very difficult to achieve densification through traditional pressureless sintering. For example, after the pressureless sintering of $B_4C$ at 2375 °C for 1 h, Roy et al. [4] achieved a relative density of only 87 %.

The sinterability and fracture toughness of $B_4C$ can be improved by introducing sintering aids such as Al, Ti, $Al_2O_3$, $ZrO_2$, and $TiSi_2$ [3,5]. Among them, $TiSi_2$ is a relatively ideal choice since $TiB_2$ and SiC formed in the in situ reaction between $TiSi_2$ and $B_4C$ can maintain the good inherent characteristics of $B_4C$, such as high hardness and low density [5]. However, even with the use of $TiSi_2$, obtaining dense $B_4C$-based ceramics through traditional pressureless sintering requires a sintering temperature of 2200 °C and a long isothermal duration of 1 h, because of sluggish atomic diffusion [5]. Hot pressing (HP) is an effective method to reduce the sintering temperature and sintering duration. For example, Xia et al. [6] obtained a relative density of 98 % by adding 11 vol% $TiSi_2$ to $B_4C$ and hot-pressing the pellets under conditions of 2000 °C-30 min-30 MPa. Similarly, Wang et al. [7] sintered $B_4C$ with 17 vol% $TiSi_2$ at 2050 °C for 15 min under 20 MPa through HP and achieved a relative density of 100 %. Despite the reduced sintering temperatures used in these studies, the temperatures still exceed 2000 °C. Furthermore, the sintering duration of conventional HP ranges from several to tens of hours because of the low heating and cooling rates, resulting in low efficiency and high energy consumption [6,7]. By contrast, Liu et al. [8] added 10 vol% $TiSi_2$ to $B_4C$ and reduced the sintering temperature and holding time in spark plasma sintering (SPS) to 1800 °C and 5 min (40 MPa). However, the high currents (thousands to tens of thousands of amperes) required for SPS lead to substantial energy consumption.

In 2020, Hu et al. [9] developed a novel ultrafast high-temperature sintering (UHS) technique, and heat was transferred by radiation and conduction. Owing to high heating rates (~$10^3$–$10^4$ °C/min) and high temperatures (≥ 1500 °C), dense oxide ceramics such as YSZ and $Al_2O_3$ could be obtained after sintering for a very short time (~10 s). Subsequently, we expanded the application of UHS to various oxides (including single and high-entropy oxides [10,11]) and non-oxides (including high-entropy carbides [12], borides [13] and nitrides [14]). Recently, Grasso et al. [15,16] prepared dense $Li_{1.5}Al_{0.5}Ge_{1.5}P_3O_{12}$ and $Li_{1.3}Al_{0.3}Ti_{1.7}(PO_4)_3$ ceramics using UHS. However, densifying ceramics with high melting points remains challenging using conventional UHS. While integrating a pressurization device into existing UHS equipment offers a potential solution, the softness of the graphite felt relative to the sample can cause issues. Direct pressure application can lead to deformation and even hole formation at contact points, resulting in non-uniform heating and damage to the graphite felt.

In this study, we present a novel Ultrafast Pressure Sintering (UPS) technique (Fig. 1(a)) using direct Joule heating to achieve rapid densification of hard-to-sinter $B_4C$-based composites at lower temperatures. The pellet was heated at a rate of 150 °C/min to 1550 °C, and maintained at this temperature for less than 2 min under a pressure of 30 MPa. Rapid and significant densification was achieved because of the formation of transient liquid phases in the reaction between $B_4C$ and $TiSi_2$ and pressure-guided particle rearrangement.

## 2. Materials and methods

### 2.1. Ultrafast pressure sintering

Commercial $B_4C$ (95 wt% purity with C and $B_2O_3$ as the main impurities, $D_{50}$ = 1.5 μm, Dunhua Zhengxing Abrasive Co., Ltd., China) and $TiSi_2$ (~95 wt% purity with free Si as the main impurity, $D_{50}$ = 2 μm, Shanghai Naiou Nano Technology Co., Ltd., China) powders were used as the raw materials. The two powders were uniformly mixed in designed proportions ($B_4C$-0/6/12/18 vol% $TiSi_2$ (based on $B_4C$)) through ball milling in a WC–Co jar. Subsequently, cylindrical pellets with dimensions of $\phi$10 mm × 3 mm were obtained under a uniaxial pressure of 400 MPa. The graphite felt was cut into the shape shown in Fig. 1(b). The center of the graphite felt was first cut to form a depression with dimensions of 32 mm × 25 mm × 5 mm, which was then split in the middle to form an open column space (diameter: ~20 mm; length: 25 mm) that extended down through the middle of the felt. Since this carbon column had higher electrical resistance than its vicinity, a concentrated zone of Joule heating could be formed. A $B_4C$ pellet was placed at the center of the lower BN block. The upper and lower BN blocks (with diameters of 20 mm) were inserted into the center hole of the graphite felt and were tightly wrapped by the graphite felt. This positioning ensured the $B_4C$ pellet remained at the center of the assembly. The outer surfaces of the upper and lower BN blocks were connected to corresponding graphite dies, which were further connected to stainless steel dies. After the furnace was evacuated to a vacuum of 5 Pa, a direct current was passed through the graphite felt and pressure was exerted on the sample according to the predetermined program. Once the desired temperature and pressure were reached, they were maintained for 0–2 min. Subsequently, the current was reduced to cool the sample and the pressure was decreased.

https://doi.org/10.1016/j.jmst.2024.05.028
1005-0302/© 2025 Published by Elsevier Ltd on behalf of The editorial office of Journal of Materials Science & Technology.

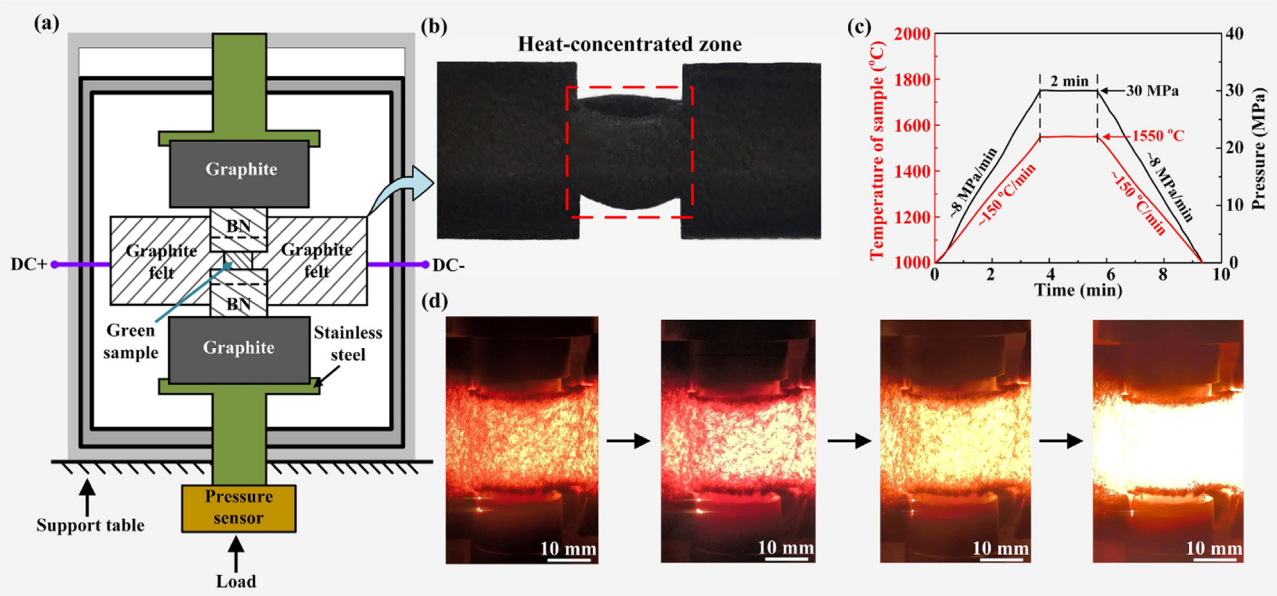


**Fig. 1.** (a) Schematic of the ultrafast pressure sintering (UPS) device from a sectional view, (b) the structure of graphite felt, (c) typical sintering and pressure curves, and (d) typical photographs taken during the UPS process.

Fig. 1 shows the structure of the graphite felt, typical sintering and pressure curves, and a schematic of the UPS device. The surface temperature of the graphite felt in the central region was measured using an infrared thermometer (E1RH, Fluke, U.S.A., temperature range: 1000–3000 °C). All temperatures reported in this paper refer to the actual sintering temperatures of the samples after calibration. Details of the temperature calibration method and data are provided in Supplementary Materials (Figs. S1 and S2).

### 2.2. Sample characterization

The chemical composition and phase structure of the samples were identified using an X-ray diffractometer (XRD; D/Max 2500 PC, Rigaku, Japan). The theoretical density of the sample was calculated using the formula:

$$\rho_{th} = \frac{m_{total}}{\frac{m_1}{\rho_1} + \frac{m_2}{\rho_2} + \cdots \frac{m_n}{\rho_n}}, \quad (1)$$

where $\rho_{th}$ is the theoretical density, $m_{total}$ is the total mass, $m_{ii=1,2,\cdots n)}$ is the mass of each phase, and $\rho_{i(i=1,2,\cdots n)}$ is the density of each phase. It is important to note that phase quantification differed based on reaction completion. For samples with incomplete reactions, the amount of each phase (excluding Si and C) was determined from the XRD patterns. Conversely, for samples with complete reactions, the quantity of each phase was calculated using the law of mass conservation. The actual densities of the samples were measured using the Archimedean method, and the relative densities were determined by calculating the ratio between the actual and theoretical densities. Additionally, the average porosity of each sample was estimated by observing ten randomly selected locations at a magnification of 200 × using an optical microscope (DSX-HRSU, Olympus Corporation, Tokyo, Japan). The reported relative densities represent the average values obtained from both the Archimedean method and porosity measurements.

Microstructural analysis was conducted using a field-emission scanning electron microscope (FESEM; JSM-7900F, JEOL, Japan) and a transmission electron microscope (TEM, JEM-2100F, JEOL, Japan) equipped with an energy dispersive spectrometer (EDS). The reaction temperature was determined using a differential scanning calorimetry (DSC) analyzer (SDT Q600, TA Instruments, USA). Nano-hardness and elastic moduli of the sintered samples were measured using a nanoindentation instrument equipped with a diamond Berkovich tip (G200, KLA-Tencor, USA). Microhardness of samples was determined using a Vickers hardness tester (HVD-1000MP, Shanghai Jvjing Precision Instrument Manufacturing Co., Ltd., Shanghai, China) at a load of 9.8 N. Finally, fracture toughness was calculated using the Anstis equation [17]

$$K_{IC} = 0.016\left(\frac{E}{H}\right)^{1/2}\frac{P}{c^{3/2}}, \quad (2)$$

where $P$ is the applied load, $E$ is the elastic modulus (obtained from the nanoindentation result), $H$ is the Vickers hardness, and $c$ is the radial crack length (measured from the indentation center).

## 3. Results and discussion

### 3.1. Phase formation and densification

As a control, a $B_4C$ pellet without any sintering aid was first sintered using pressureless ultrafast high-temperature sintering. This process involved sandwiching the $B_4C$ pellet between two Joule-heated graphite felts, as described in our previous work [10]. However, even after sintering at 2100 °C for 2 min, the relative density of the sample reached only 57 %. In order to improve sinterability, $TiSi_2$ (melting point: 1489 °C) was added to the $B_4C$ pellet and the experiment was repeated. As shown in Fig. S3, the relative density of the $B_4C$-18 vol% $TiSi_2$ composite reached 65 %. XRD results (Fig. S4) confirmed that $TiSi_2$ had completely reacted with $B_4C$ to form SiC and $TiB_2$. The limited improvement in the density of $B_4C$, despite the introduction of $TiSi_2$, is likely attributed to insufficient particle rearrangement under pressureless sintering conditions, since liquid-phase $TiSi_2$ was short-lived.

In order to further improve the sinterability, we developed the UPS technique with the device schematically shown in Fig. 1(a). The $B_4C$-18 vol% $TiSi_2$ system was chosen to examine the effect of applied pressure ($P$). Fig. 2($a_1$–$a_4$) demonstrates that increasing the applied pressure significantly increased the relative density of the $B_4C$ pellet. Notably, at a sintering temperature ($T$) of 1550 °C

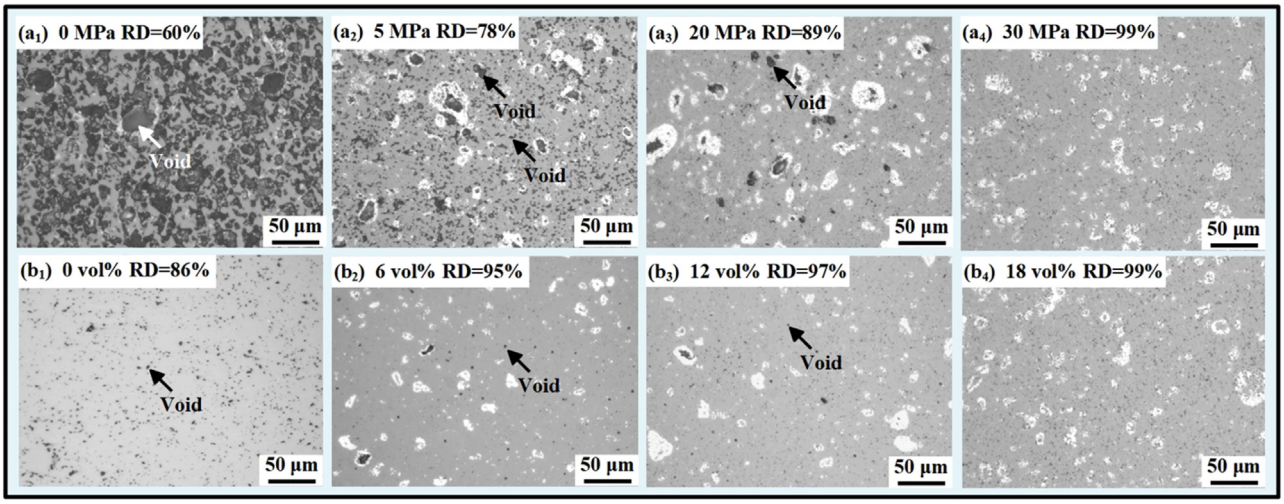


**Fig. 2.** Optical micrographs of polished surfaces of samples sintered ($a_1$–$a_4$) under different applied pressures and ($b_1$–$b_4$) with different $TiSi_2$ contents (1550 °C, 2 min; secondary phases are white or grey in color, while pores are darker; RD means relative density).

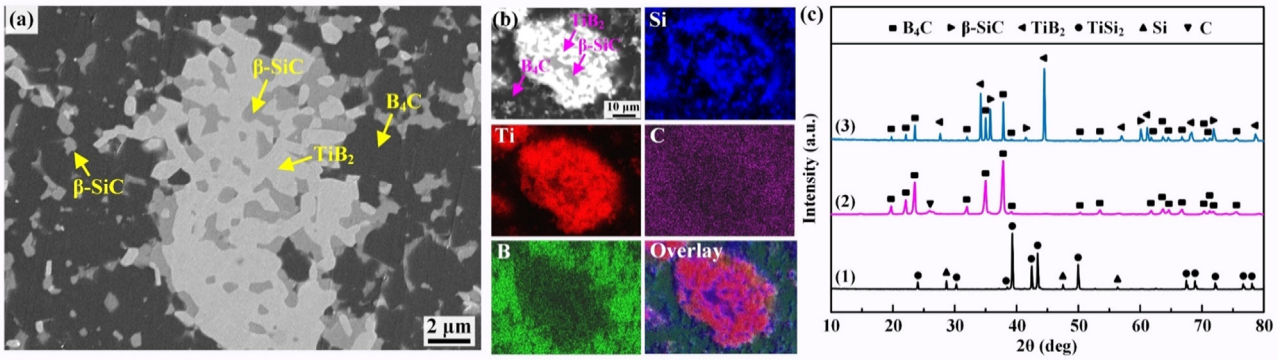


**Fig. 3.** (a) FESEM image of the sintered sample, (b) FESEM image and the corresponding element distribution map of the sample in the BSE mode, and (c) XRD patterns of (1) $TiSi_2$ powder, (2) $B_4C$ powder, and (3) the sintered sample (1550 °C, 18 vol% $TiSi_2$, 30 MPa, 2 min).

and a pressure ($P$) of 30 MPa, the relative density of the specimen approached 100 % (Fig. 2($a_4$)).

To investigate the effect of $TiSi_2$ content, the temperature, pressure, and dwell time (the duration for which temperature and pressure were maintained) were fixed at 1550 °C, 30 MPa, and 2 min, respectively. Under these conditions, the relative density of a pure $B_4C$ sample after UPS was 86 % (Fig. 2($b_1$)). With an increase in the $TiSi_2$ content, the relative density increased (Fig. 2($b_1$–$b_4$)). When the $TiSi_2$ content reached 18 vol%, the sample was almost fully densified (Fig. 2($b_4$)). SEM and XRD analyses (Fig. 3) indicate that secondary phases (SiC and $TiB_2$) were present in the sample, and $TiSi_2$ had been completely consumed. To further investigate the microstructure with higher resolution, TEM analyses were performed, and the results are presented in Fig. 4. These analyses confirmed the presence of $B_4C$, SiC, and $TiB_2$, consistent with the SEM and XRD findings.

### 3.2. Mechanisms for reaction and densification

Fig. 5(a) depicts the DSC curve of the as-pressed $B_4C$-18 vol% $TiSi_2$ pellet. An exothermic peak and an endothermic peak are apparent at $T$ = 660 °C and 1338 °C, respectively. The exothermic peak may be attributed to the surface oxidation of $B_4C$ powder, while the endothermic peak is possibly related to the eutectic reaction between $TiSi_2$ and Si (eutectic temperature: 1330 °C (Fig. S5)).

In order to determine the reaction process during UPS, we interrupted the experiments at several representative stages by switching off the power and unloading the applied pressure. Fig. 5(b and c) shows no significant reaction between $B_4C$ and $TiSi_2$ at temperature below 1000 °C (note that the measurement range of the infrared thermometer used in this study is 1000–3000 °C. Therefore, for temperatures below 1000 °C, the exact values cannot be accurately determined, and the term "$T$ < 1000 °C" is used to represent these cases). At 1200 °C, the intensity of the $TiSi_2$ peak decreased, while that of the Si peak increased (Fig. 5(b)), and small amounts of $TiB_2$ and SiC were observed locally (Fig. 5(d)). Between 1350–1400 °C, $TiSi_2$ was completely consumed, and the content of $TiB_2$, SiC, and Si increased (Fig. 5(b)). In addition, at 1350 °C, distinct $TiB_2$-SiC agglomerates appeared around the pores (Fig. 5(e)), likely due to the formation of a $TiSi_2$-Si eutectic liquid phase (eutectic temperature 1330 °C). This liquid phase then flowed outward and reacted with surrounding $B_4C$ particles. At 1450 °C, fine SiC phases were observed at the edges of the $B_4C$ particles in addition to blocky $TiB_2$-SiC phases (Fig. 5(f)). After the sample was sintered at 1550 °C under 30 MPa, XRD analysis (Fig. 5(b)) revealed the presence of only $B_4C$, SiC, and $TiB_2$.

Based on these results, the proposed reaction process involves (1) Solid-state contact reaction between $B_4C$ and $TiSi_2$ to form $TiB_2$, SiC, and Si ($B_4C + 2TiSi_2 \rightarrow 2TiB_2 + SiC + 3Si$); (2) Eutectic reaction between $TiSi_2$ and Si (from impurities and the solid-state reaction) as temperature and pressure increase, forming a liquid phase that accelerates the reaction with $B_4C$; (3) Reaction of molten Si

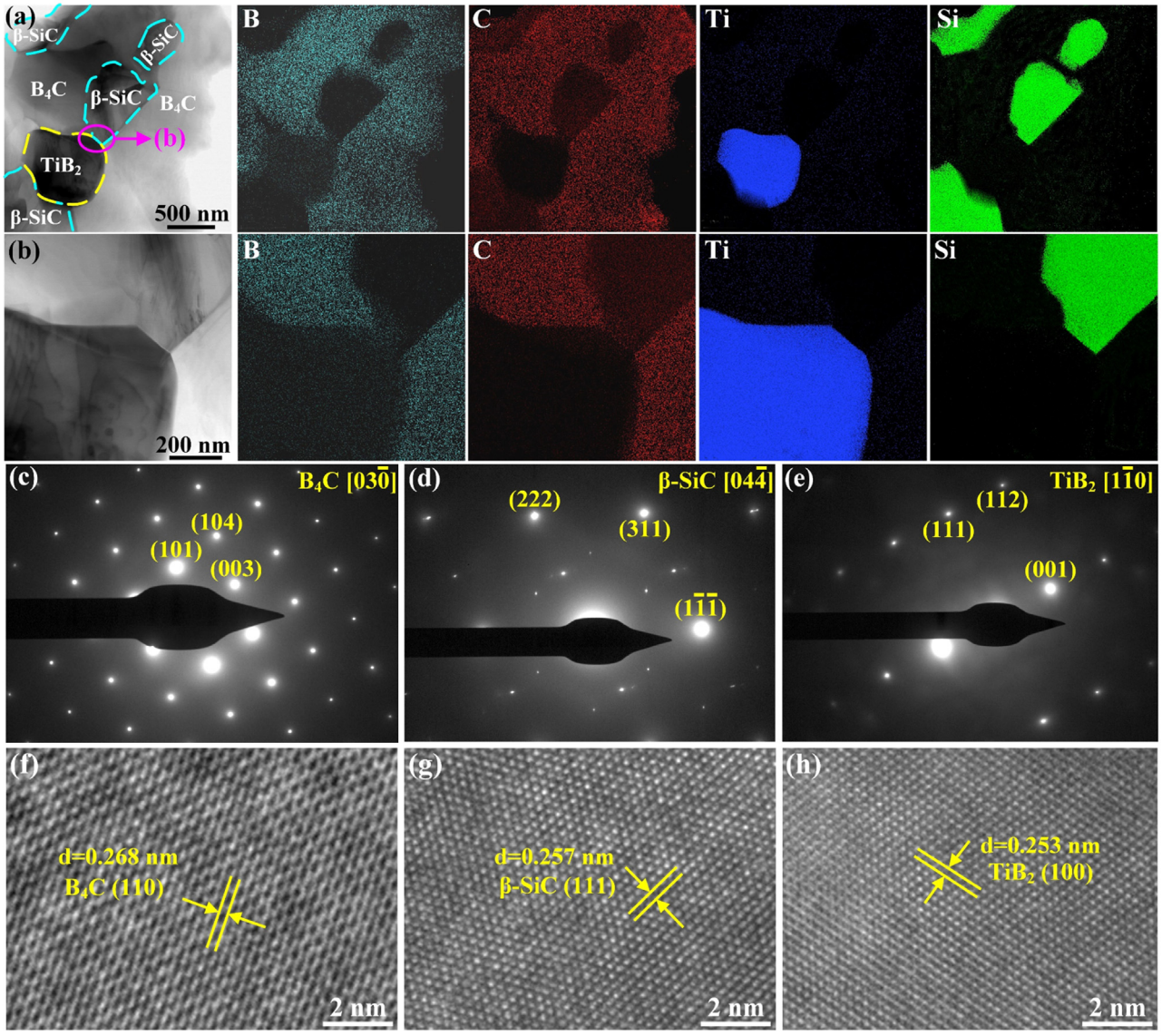


**Fig. 4.** (a) TEM image and corresponding elemental distribution of the sintered sample, (b) partially enlarged TEM image of (a), (c–e) SAED patterns and (f–h) HRTEM images (1550 °C, 18 vol% $TiSi_2$, 30 MPa, 2 min).

($T$ > 1410 °C) with C to form SiC (Si(l) + C → SiC), with C sourced from $B_4C$ raw powder impurities; (4) Rapid consumption of $TiSi_2$ and transformation into $TiB_2$ and SiC, as supported by thermodynamic calculations (Fig. S6).

The formation of the $TiSi_2$-Si eutectic liquid phase played an important role in the densification of $B_4C$ during UPS. As shown in Fig. 5(g, i–iii), in the case of a high heating rate (150 °C/min), rigid ceramic skeletons could not form between $B_4C$ particles before the formation of the eutectic liquid phase. The eutectic liquid phase, which served as a lubricant, reduced the friction during the rotation and sliding of $B_4C$ particles. As a result, $B_4C$ particles rearranged significantly under the action of pressure. Furthermore, the good wettability between $B_4C$ and the eutectic liquid phase facilitated the infiltration of the liquid into the gaps between $B_4C$ particles and promoted the reaction [8]. Therefore, when the sintering temperature was increased from 1200 to 1400 °C, the relative density of the sample increased significantly from 49 % to 89 % (Fig. S7). With a further increase in the sintering temperature to 1550 °C, the Si liquid phase filled residual pores and reacted with C (Fig. 5(g, iv)). Consequently, nearly fully dense $B_4C$ was obtained after sintering at 1550 °C without any dwelling stage (Fig. 5(g, v) and S7).

### 3.3. Mechanical properties

The hardness, elastic moduli, and fracture toughness of samples with different $TiSi_2$ contents were determined using the indentation method. With an increase in the $TiSi_2$ content, the nano- and Vickers hardness of the sintered body decreased, while the elastic modulus and fracture toughness increased (Table 1). The decrease in the hardness is primarily attributed to the relatively lower intrinsic hardness of the newly formed SiC and $TiB_2$ phases (Table 1). The elastic modulus of $B_4C$ is close to that of SiC but significantly lower than that of $TiB_2$ (Table 1). Consequently, increasing the $TiB_2$ content led to higher elastic moduli of the sintered samples. The enhancement of fracture toughness is mainly attributed to two aspects. First, crack deflection caused by the newly formed $TiB_2$ phase played a significant role. In the pure $B_4C$ sample, crack propagation was relatively straight; whereas in the $B_4C$-$TiB_2$-SiC sample, crack deflection occurred at phase boundaries (Fig. 6).

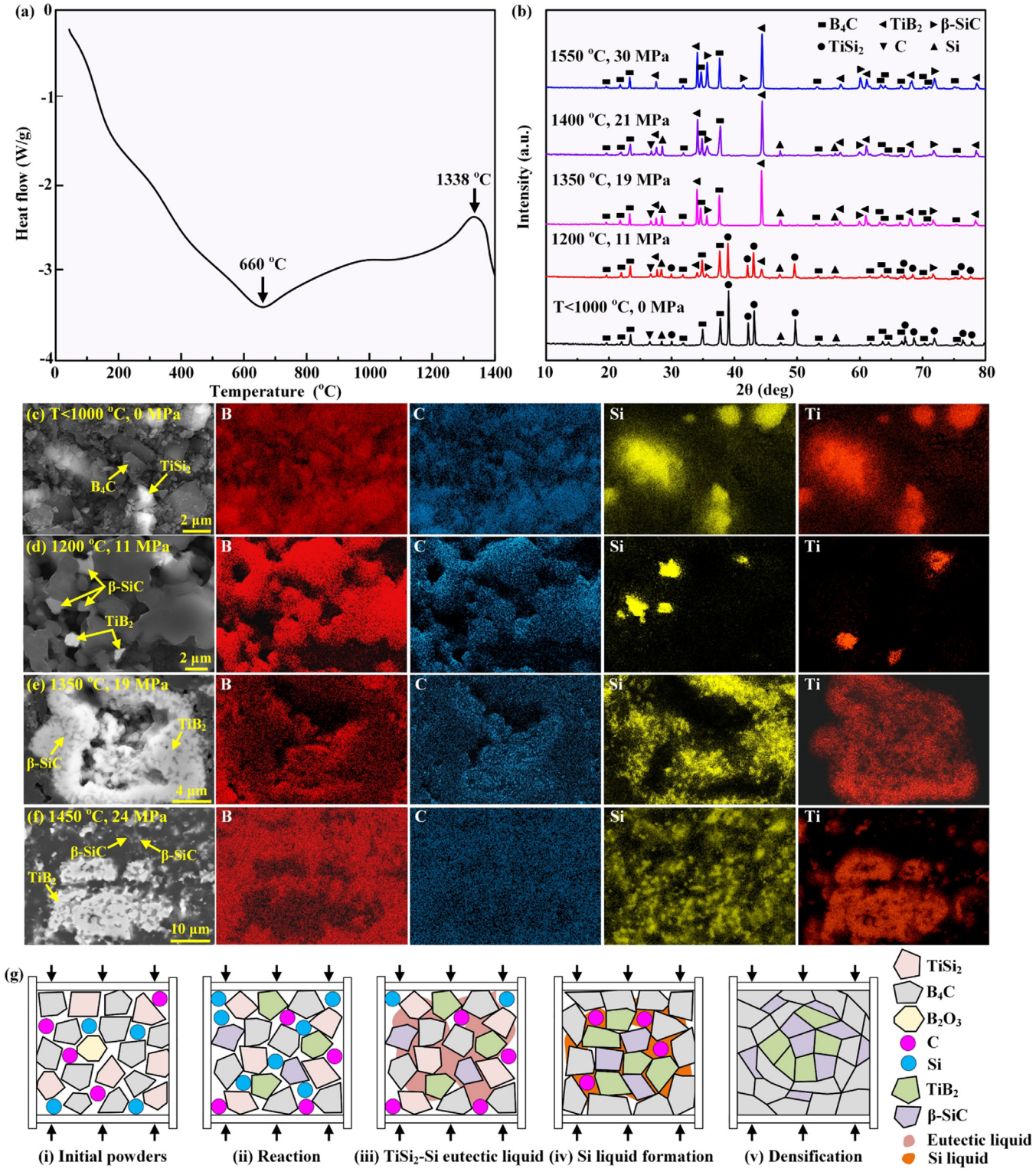


**Fig. 5.** (a) DSC curve of the $B_4C$-18 vol% $TiSi_2$ pellet (Ar atmosphere, flow rate: 20 ml/min, heating rate: 10 °C/min), (b) XRD patterns of samples from interrupted experiments, (c–f) FESEM images and corresponding elemental distribution of samples from interrupted experiments, and (g) schematic of reaction and densification processes.

This phenomenon may be related to the residual stress between different phases, as the thermal expansion coefficients (TECs) of $B_4C$ and SiC are similar, while those of $B_4C$ and $TiB_2$ differ significantly (Table 1). As a result, crack deflection occurred around $TiB_2$ particles, dissipating most of the fracture energy and increasing the fracture toughness. Second, the intrinsic fracture toughness of SiC is higher than that of $B_4C$ (Table 1), which is conducive to the improvement of fracture toughness [8]. Furthermore, residual stresses generated during cooling from elevated temperatures can influence mechanical properties. The phase with a higher TEC experiences tensile stress, potentially promoting crack propagation and reducing hardness and fracture toughness. In contrast, the

**Table 1**
Mechanical and thermal properties of $B_4C$, $TiB_2$, and SiC (obtained from the literature) and mechanical properties of $B_4C$ and $B_4C$-based composites prepared through UPS.

| Material | Vickers hardness (GPa) | Nano-hardness (GPa) | Elastic modulus (GPa) | Fracture toughness ($MPa{\cdot}m^{1/2}$) | Thermal expansion coefficient ($K^{-1}$) |
|---|---|---|---|---|---|
| $B_4C$ | 32 [18] | – | 445 [18] | 1.9 [2] | $4.5 \times 10^{-6}$ [8] |
| $TiB_2$ | 25 [19] | – | 671 [21] | 3.3 [22] | $8.1 \times 10^{-6}$ [8] |
| $\beta$-SiC | 26 [20] | – | 420 [21] | 4.5 [20] | $4.4 \times 10^{-6}$ [8] |
| $B_4C$ | 32.6 ± 1 | 39.8 ± 2 | 430 ± 13 | 1.6 ± 0.3 | – |
| $B_4C$-6 vol% $TiSi_2$ | 31.8 ± 1 | 39.2 ± 2 | 436 ± 13 | 2.0 ± 0.2 | – |
| $B_4C$-12 vol% $TiSi_2$ | 31.2 ± 1 | 38.5 ± 2 | 444 ± 14 | 2.6 ± 0.3 | – |
| $B_4C$-18 vol% $TiSi_2$ | 30.5 ± 1 | 37.3 ± 2 | 448 ± 14 | 3.1 ± 0.2 | – |

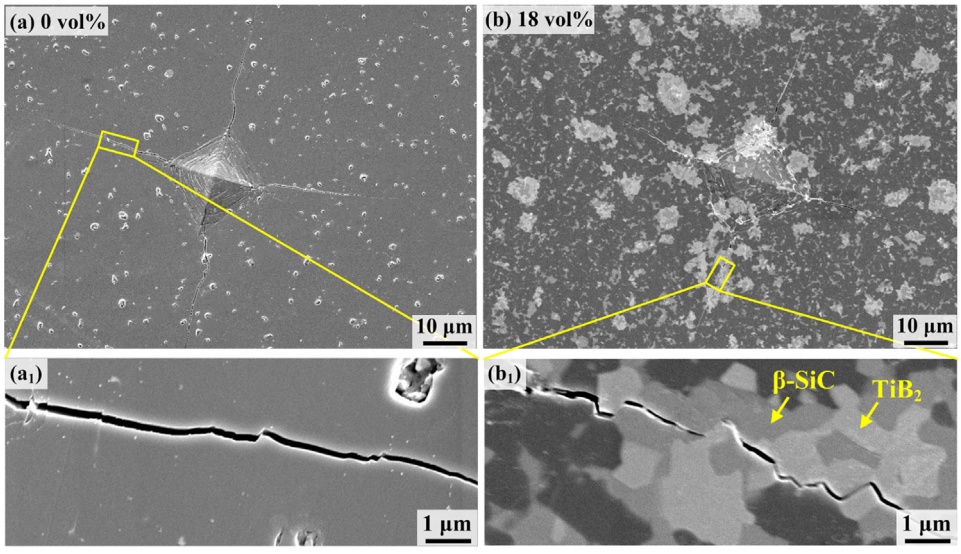


**Fig. 6.** (a, b) Vickers indentations and ($a_1$, $b_1$) crack propagation in pure $B_4C$ and $B_4C$-$TiB_2$-SiC (from $B_4C$-18 vol% $TiSi_2$) samples.

phase with a lower TEC undergoes compressive stress, which can suppress crack propagation and enhance these properties [23–26]. Although the effects of residual stresses are not as pronounced as the intrinsic phase properties, they may contribute to the observed differences in mechanical properties compared to those reported in the literature.

## 4. Conclusions

We developed a new method, termed ultrafast pressure sintering (UPS), to achieve the low-temperature and ultrafast densification of $B_4C$-based ceramics. The green bodies were directly heated at a rate of 150 °C/min using the Joule heat generated by the electrified graphite felt. Under a 30 MPa pressure, nearly fully dense $B_4C$ was obtained at 1550 °C within 2 min. The rapid densification is mainly attributed to the relatively high heating rate of UPS, particle rearrangement and pore filling caused by the combined effects of pressure and transient liquid phases, as well as mass transport promoted by the rapid reaction between $B_4C$ and $TiSi_2$. In particular, the newly formed $TiB_2$ and SiC phases significantly enhanced the fracture toughness of $B_4C$. The proposed UPS method offers several advantages, such as simplicity, efficiency, and energy savings, and paves the way for the rapid densification of bulk ceramics.

## Declaration of competing interest

The authors declare that they have no known competing financial interests or personal relationships that could have appeared to influence the work reported in this paper.

## CRediT authorship contribution statement

**Yu Sun:** Writing – original draft, Software, Methodology, Investigation. **Xiang-Yu Bai:** Methodology. **Rui-Fen Guo:** Resources. **Ping Shen:** Writing – review & editing, Resources.

## Acknowledgment

This work is supported by the National Natural Science Foundation of China (No. 52372061) and the Project of the Education Department of Jilin Province (No. JJKH20231163KJ).

## Supplementary materials

Supplementary material associated with this article can be found, in the online version, at doi:10.1016/j.jmst.2024.05.028.

## References

[1] F. Thevenot, J. Eur. Ceram. Soc. 6 (1990) 205–225.
[2] A.K. Suri, C. Subramanian, J.K. Sonber, T.S.R.C. Murthy, Int. Mater. Rev. 55 (2010) 4–40.
[3] W. Zhang, S. Yamashita, H. Kita, Adv. Appl. Ceram. 118 (2019) 222–239.
[4] T.K. Roy, C. Subramanian, A.K. Suri, Ceram. Int. 32 (2006) 227–233.
[5] S. Wang, L. Li, S. Yan, Y.Y. Deng, S.B. Gao, P.F. Xing, J. Mater. Res. Technol. 9 (2020) 8685–8696.
[6] T. Xia, X.S. Tu, F. Zhang, J.Y. Zhang, Li. Ren, J. Wuhan Univ. Technol. Mater. Sci. Ed. 38 (2023) 12–19.
[7] S. Wang, Y.Y. Deng, S.B. Gao, M.S. Yang, P.F. Xing, Int. J. Appl. Ceram. Technol. 17 (2020) 2569–2579.
[8] Y. Wang, Q. Liu, B. Zhang, H.Q. Zhang, Y.C. Jin, Z.X. Zhong, J. Ye, Y.H. Ren, F. Ye, W. Wang, Ceram. Int. 47 (2021) 10665–10671.

[9] C. Wang, W. Ping, Q. Bai, H. Cui, R. Hensleigh, R. Wang, A.H. Brozena, Z. Xu, J. Dai, Y. Pei, C. Zheng, G. Pastel, J. Gao, X. Wang, H. Wang, J.C. Zhao, B. Yang, X.R. Zheng, J. Luo, Y. Mo, B. Dunn, L. Hu, Science 368 (2020) 521–526.
[10] R.F. Guo, H.R. Mao, Z.T. Zhao, P. Shen, Scr. Mater. 193 (2021) 103–107.
[11] Z.T. Zhao, R.F. Guo, H.R. Mao, P. Shen, J. Eur. Ceram. Soc. 41 (2021) 5768–5773.
[12] H.R. Mao, E.T. Dong, S.B. Jin, X.M. Qiu, P. Shen, J. Eur. Ceram. Soc. 42 (2022) 4053–4065.
[13] R.F. Guo, H.R. Mao, P. Shen, J. Eur. Ceram. Soc. 43 (2023) 5763–5773.
[14] T. Che, H.R. Mao, R.F. Guo, P. Shen, Ceram. Int. 49 (2023) 31530–31538.
[15] J.H. Wu, Y. Lin, M. Kermani, C.F. Hu, S. Grasso, Ceram. Int. 48 (2021) 6356–6362.
[16] Y. Lin, N. Luo, E. Quattrocchi, F. Ciucci, J.H. Wu, M. Kermani, J. Dong, C.F. Hu, S. Grasso, Ceram. Int. 47 (2021) 21982–21987.
[17] S. Liu, W.T. Hu, J.Y. Xiang, Ceram. Int. 40 (2014) 10517–10522.
[18] B.M. Moshtaghioun, A.L. Ortiz, D. Gómez-García, A. Domínguez-Rodríguez, J. Eur. Ceram. Soc. 33 (2013) 1395–1401.
[19] G.B. Raju, A. Mukhopadhyay, K. Biswasb, B. Basua, Scr. Mater. 61 (2009) 674–677.
[20] H. Kodama, T. Miyoshi, J. Am. Ceram. Soc. 73 (1990) 3081–3086.
[21] M. Iuga, G. Steinle-Neumann, J. Meinhardt, Eur. Phys. J. B 58 (2007) 127–133.
[22] G.L. Zhao, C.Z. Huang, H.L. Liu, B. Zou, H.T. Zhu, J. Wang, Ceram. Int. 40 (2014) 2305–2313.
[23] O.L. Ighodaro, O.I. Okoli, Int. J. Appl. Ceram. Technol. 5 (2008) 313–323.
[24] C.H. Xu, Ceram. Int. 31 (2005) 537–542.
[25] Y. Wan, J.H. Gong, Mater. Lett. 57 (2003) 3439–3443.
[26] D. Kovar, S.J. Bennison, M.J. Readey, Acta Mater. 48 (2000) 565–578.

Yu Sun
Xiang-Yu Bai
Rui-Fen Guo*
Ping Shen*
*Key Laboratory of Automobile Materials (Ministry of Education), School of Materials Science and Engineering, Jilin University, No. 5988 Renmin Street, Changchun 130025, China*
*Corresponding authors.
*E-mail addresses:* guoruifen@jlu.edu.cn (R.-F. Guo), shenping@jlu.edu.cn (P. Shen)
Revised 18 May 2024